JMEPEG (2021) 30:2449–2461
https://doi.org/10.1007/s11665-021-05523-8

1059-9495/$19.00

Influence of WC Particle on the Metallurgical, Mechanical, and Corrosion Behavior of AlFeCuCrCoNi-WC_x High-Entropy Alloy Coatings

Akash Vyas, Jyoti Menghani, and Harshad Natu

Submitted: 24 August 2020 / Revised: 6 December 2020 / Accepted: 23 January 2021 / Published online: 10 March 2021

The high-entropy alloy AlFeCuCrCoNi-WC_x (x = 5, 10, and 15 wt.%) multi-principal element claddings were synthesized with the aid of laser-assisted cladding process on AISI 316 steel substrate. The microstructural behavior was characterized by optical microscopy, field emission scanning electron microscope equipped with energy dispersive spectroscopy (FESEM/EDS). The phase analysis using XRD revealed that in addition to the combination of two FCC + BCC phases, a set of diffraction peaks corresponding to WC and $Cr_{23}C_6$ phases is observed. The observation indicates that the cladding zone is mainly consisting of fine-grained nondirectional and equiaxed crystals away from the base material and columnar grains near to the base material. Microstructural observations also conclude that increasing WC leads to refinement in the grain size. The formation of chromium carbide is limited to the AlFeCuCrCoNi-WC_{10} AlFeCuCrCoNi-WC_{15} high-entropy alloy coatings due to insufficient carbon content in AlFeCuCrCoNi-WC_5 high-entropy alloy coatings to form chromium carbide. As compared to the substrate AISI 316 (164.5 $HV_{0.5}$), the microhardness of the AlFeCuCrCoNi-WC_5, AlFeCuCrCoNi-WC_{10} and AlFeCuCrCoNi-WC_{15} claddings is enhanced by approximately 49.6%, 73.5% and 79.7%, respectively. The corrosion resistance of the AlFeCuCrCoNi-WC_x multi-principal element coating in 3.5 wt.% NaCl corrosive environment is better than that of the substrate AISI 316. However, the corrosion rate of the high-entropy alloy coating increases and corrosion resistance is deteriorated with the rise in WC content.

Keywords corrosion resistance, high-entropy alloy, laser cladding, microhardness, microstructure, XRD

1. Introduction

Failure due to corrosion, wear, and fatigue accounts for nearly all the surfaces of industrial machineries working under adverse circumstances. Furthermore, tribology as well as corrosion and fatigue resistance as combined properties are essential in several applications. The example includes an aggressive environment endured by pumps in chemical industries, the bearings and gears in naval aircraft energy generators located in seawater (as a marine environment-friendly renewable energy source) are attacked by chloride ions (Ref 1, 2).

In order to overcome the mentioned complications, researchers pay much attention to surface engineering in recent time (Ref 3, 4). High-power CO_2 lasers find applications in many types of metal processing, such as cutting, welding, and surface treatments. The latter group includes surface cladding, which is a technique to provide a metal substrate with wear and corrosion-resistant layer. The laser surface cladding enables the production of surface layers having properties like fine grain (grain refinement due to rapid cooling rate) and prevents component segregation and at the same time has excellent metallurgical bonding to the substrate, full dense coating layer, and minimal effect on the bulk properties of the substrate (Ref 5, 6). The coating synthesizes through the laser-cladding process exhibits better characteristics in terms of the small heat-affected zone, optimum dilution, rapid solidification rate, and excellent metallurgical bonding than those produced by plasma arc (Ref 7), magneto sputtering (Ref 8), and electrochemical deposition (Ref 9).

Among the various compositions of coating materials, the high-entropy alloys (HEA) exhibit outstanding corrosion resistance and mechanical properties. The high-entropy alloy is a novel type of alloy system invented in recent years. These alloys consist of multiple principal elements in equimolar/equiatomic or near equimolar/equiatomic ratios, each at 5-35 atomic fractions. Due to the high mixing entropy, these alloys are generally composed of a single solid solution phase rather than complex brittle intermetallic (Ref 7–9). The multiple elements with proper composition may offer high-entropy alloys with a wider range of applications due to high hardness and mechanical strength along with excellent wear resistance (Ref 10), distinctive electrical and magnetic properties (Ref 11), good erosion resistivity as well as excellent thermal stability (Ref 12–14). The phenomena behind these superior characteristics compared to conventional alloy is four core effect namely (a) High-entropy effect: high entropy tends to stabilize solid solution phases, (b) Sluggish diffusion effect: diffusion coefficients of multiple elements are lower than in pure metals and conventional alloy, (c) Cocktail effect: unexpected properties,

Akash Vyas and **Jyoti Menghani**, Mechanical Engineering Department, Sardar Vallabhbhai National Institute of Technology (SVNIT), Surat 395007, India; and **Harshad Natu**, Magod Fusion Technologies Private Limited, Pune 4?1026, India. Contact e-„mail: akku.vyas2011@gmail.com.

which cannot be attributed to any of the independent components can occur and (d) Severe lattice distortion effect: numerous atoms are randomly distributed in a crystal lattice, leading to lattice distortion what results in increased strength of the alloys and slower kinetics of transport processes (Ref 15–19).

In many tribological applications, high-entropy alloy coatings are widely used because of their high hardness and excellent wear resistance. However, few high-entropy alloys have low hardness and yield strength (200-300 MPa) (Ref 20). Inclusion of ceramic particles, such as WC, TiC and SiC, in the coating is common for nickel, cobalt, or iron-based alloy. However, there are few investigations on laser-cladded high-entropy alloy coatings strengthened by reinforcing phase elements. WC has a very high hardness (2600 HV) and melting point (2600 °C), making it ideal as a reinforcement material (Ref 21–23). Considering the case of AlCrFeNiCoCu high-entropy alloy prepared by powder metallurgy Process, EDS analysis indicated the composition segregation in the alloy and microstructure is classified into in to three parts, amplitude modulation-like, point-like and fibrous regions. Al, Cr, Cu, and Fe are segregated in the alloy and form micro etching batteries, which accelerate the corrosion rate. However, the Cr content in point-like microstructure has exceeded the critical value (18% Cr) for passivation, which contributes to the excellent corrosion resistance in the 1 mol L^{-1} NaCl solution. Considering this as basis for the selection of present system and with aim to have excellent mechanical and corrosion properties simultaneously, WC was added in the high-entropy alloy system (Ref 24).

Austenitic stainless steels are widely used due to their high corrosion resistance, but their relatively poor tribological properties still limit their fields of application. However, in addition to the moderately high corrosion rate of AISI 316 in slow-moving seawater, it has low resistance to pitting and crevice corrosion (Ref 25). The paper presents a detailed investigation of AlFeCuCrCoNi-WC_x high-entropy alloy coating on the AISI 316 substrate through a laser-cladding process. The microstructure, microhardness, phase constituents as well as chemical composition of the high-entropy alloy coatings investigated briefly. Furthermore, an in-depth investigation is carried out to determine the corrosion performance of AlFeCuCrCoNi-WC_x HEA coating in comparison with substrate AISI 316 in 3.5 wt.% NaCl corrosive environment.

2. Materials and Methods

2.1 Preparation of Coating

As received, AISI 316 steel in the form of a plate with the dimensions of 40 mm × 20 mm × 10mm was used as the substrate material. The high input laser energy may lead to distortion of large size substrate during laser-cladding process if clamping is not done properly. To avoid this type of experimental inconvenience, small size of the substrate is selected. The nominal chemical composition of the substrate in wt.% is shown in Table 1. The substrate was polished with 800 grit size emery paper to reduce laser reflectivity and was cleaned with acetone before deposition. As a cladding material, an equiatomic Al, Fe, Cr, Co, Ni, and Cu metal powders with a reinforcement of 5, 10, and 15 wt.% tungsten carbide particles were used. The particle size of the powder is between 80 and 100 mesh size with a purity of 99.9%. The intention behind choosing a specific individual element for the preparation of multi-principal element alloy is mixing enthalpy between elemental pair, as listed in Table 2 (Ref 15, 26).

2.2 Laser Cladding

The powder utilized for the preparation of high-entropy alloy (AlFeCuCrCoNi-WC_x) in the present investigation were mixed homogeneously in 3D Multi-Motion Mixer (Alphie 0.3 Hp) for 30 min (15 min forward and 15 min reverse cycle). A 4kW CO_2 laser system located at the Magod Fusion Technology, Pune (as shown in Fig. 1a) was used to deposit the cladding layer on the substrate. The process parameters of the laser-assisted cladding process were as listed in Table 3, whereas a 60% overlap condition for multi-tracking was employed. During laser-cladding process, we need to overlap cladding layers for the continuous cladding as shown in below Fig. 1(b). As you can see from Fig. 1(c), and (d) increasing in overlapping ration reduce the magnitude of the surface roughness. On the other hand, increasing in overlapping ratio leads to reduce dilution and it may affect the bonding strength between substrate and cladding layer. Furthermore, 60% overlapping ratio (O_R) is found to be ideal to maintain surface roughness as well as dilution of the clad layer (Ref 27). The

Table 1 Chemical content of AISI 316 steel (wt.%)

Elements	Ni	Mo	P	S	N_2	C	Mg	Si	Cr	Fe
Composition	10.0-14.0	2.00-3.00	0.045	0.03	0.1	0.08	2.00	0.1	16.0-18.0.	65-70

Table 2 Binary mixing enthalpies, $\Delta H^{mix}ij$ (kJ mol^{-1}) of high-entropy alloy (Ref 15, 26)

Elements	Al	Fe	Ni	Cu	Cr	Co	W	C
Al	…	− 11	− 22	− 1	− 10	− 19	− 2	− 30
Fe	− 11	…	2	13	− 1	− 1	4	− 50
Ni	− 22	2	…	4	− 7	0	− 9	− 30
Cu	− 1	13	4	…	12	6	23	− 42
Cr	− 10	− 1	− 7	12	…	− 4	5	− 61
Co	− 19	− 1	0	6	− 4	…	− 5	− 42
W	− 2	4	− 9	23	5	− 5	…	− 32
C	− 30	− 50	− 30	− 42	− 61	− 42	− 32	…

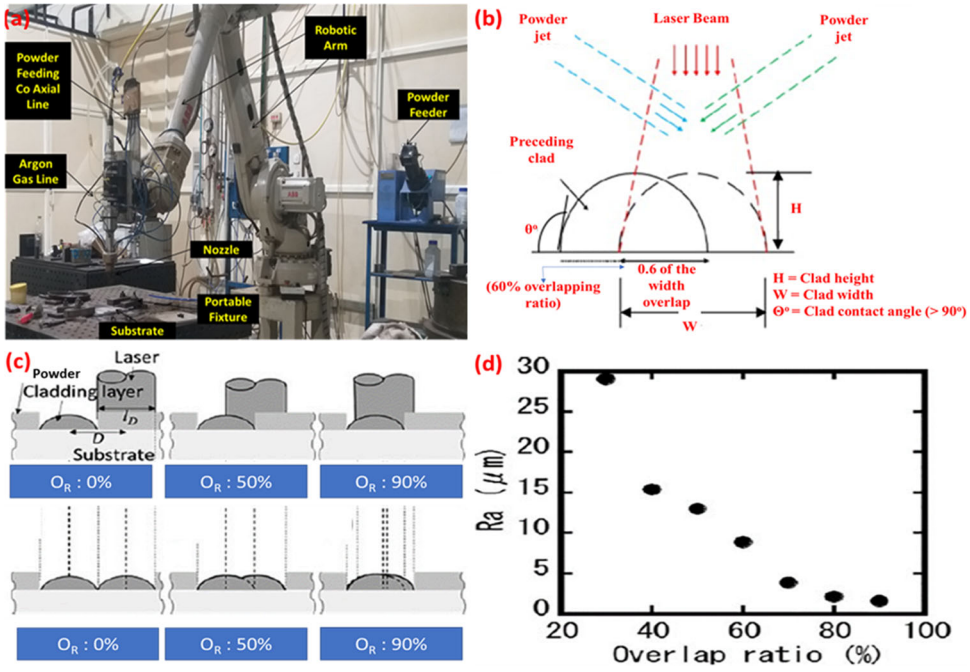

Fig. 1 (a) Laser-cladding experimental setup, (b) clad profile with overlapping details, (c) schematic diagram of effect of overlapping ration on surface roughness, O_R = 0%, O_R = 50% and O_R = 90%, (d) variation of surface roughness as function of overlapping ratio (Ref 27)

Table 3 Laser-cladding operating factors

Operating factors	Magnitude
Scanning/travel velocity, mm min^{-1}	500
Powder feed rate, g min^{-1}	4
Laser power, kW	1.1
Spot diameter, mm	2.4
Argon flow rate, L min^{-1}	6
Standoff distance, mm	8

pure argon gas was supplied at the flow rate of 6 L min^{-1} to avoid oxidation during the experiment.

2.3 Metallurgical and Mechanical Characterization

The cladded samples were prepared for metallographic examination, and steps involved were sectioning perpendicular to the laser scanning direction, mounting in bakelite followed by grinding, polishing, and etching with an aqua regia solution. The variation in the clad microstructure starting from the cladding zone followed by interface zone and substrate was observed by optical microscopy (Leica S8APO) and field emission scanning electron microscope (FESEM-JSM7100F), respectively. Furthermore, Microcam 4.1 software equipped with an optical microscope was used to determine the average grain size of individual coatings. The compositional analysis of high-entropy alloy cladded specimens carried out with the help of an energy dispersive spectrometer (EDS). The X-ray diffraction (XRD) analysis was carried out with the aid of RIGAKU diffractometer along with Cu Kα radiation, and further origin 8.0 software was used to plot the data obtain from the XRD. The microhardness of the cladding layers from the coating surface to the substrate was determined using a micro vickers hardness tester (Future Tech Corporation, Japan –FM 700) applying a load of 0.5 Kg with a dwell time of 15 s. The distance between two progressive indentations was 200 μm.

2.4 Electrochemical Characterization

The specimens used for electrochemical characterization were polished utilizing SiC emery papers from 320 to 1200 grit. The average roughness values (Ra = 0.3 μm) of these specimens were quantified with the aid of Mitutoyo SJ-411, Mitutoyo, precision surface roughness tester. The corrosion behavior of AlFeCuCrCoNi-WC_x HEA coating and base material AISI 316 stainless steel in 3.5 wt.% NaCl corrosive solution was thoroughly investigated with the help of CHI608C (CH Instruments-680 Amp Booster) potentiodynamic polarization system at 25 °C under atmospheric pressure. In an electrochemical device, the working electrode is the electrode on which the reaction of interest takes place. In a configuration of three electrodes, the operating electrode (working electrode) is often used in combination with counter electrode and a reference electrode. The working electrode is called cathodic or anodic, respectively, depending on whether the reaction on the electrode is a reduction or an oxidation. In present investigation we want to determine the corrosion behavior of high-entropy alloy coating. Therefore, in the three-electrode standard cell the coating is used as working electrode. The saturated calomel and platinum electrodes were used as reference electrode and counter electrode, respectively. The ultra-pure deionized water from Millipore (Merck-F6PA33269F) was used as an electrolyte. The calibration was conducted in accordance with ASTM standards G59. The surface area of $1cm^2$ of cladded specimen and substrate AISI 316 was investigated for corrosion study. The open-circuit potential (OCP) was stabilized for 1 hour before initiating the actual polarization scan. The spec-

imen was scanned potentiodynamically with a scanning rate of 1 mV s^{-1} (Scanning range: − 0.8 to 0.8 V). The electrochemical parameters, such as corrosion current ($I_{corr.}$), corrosion potential ($E_{corr.}$), and corrosion rate, are obtained with the help of the Tafel extrapolation method. The field emission scanning electron microscopy (FESEM- JSM7100F) is used to observe the surface morphology of the corroded substrate as well as cladded specimen.

3. Results and Discussion

3.1 XRD Spectra Analysis

Figure 2 indicates the X-ray diffraction profiles of all three coatings, including AlFeCuCrCoNi-WC_5, AlFeCuCrCoNi-WC_{10} and AlFeCuCrCoNi-WC_{15}. The crystal structure of rapidly solidified high-entropy alloy coating found to be a simple solid solution with a combination of both phases FCC and BCC. Figure 2 also depicts that in addition to the combination of two phases FCC (JCPDS: 65-5171) + BCC (JCPDS: 65-3201), an additional set of diffraction peaks corresponds to WC (JCPDS: 51-0939) phases and metal carbide phases are observed. As the XRD results depict that the scattering intensity of BCC phase is much higher than that of FCC phase, it can be concluded that the BCC solid solution phase is the primary phase (Ref 28). Furthermore, an individual fraction of phase in high-entropy alloy cladding can be calculated by the aid of the following equations (Ref 29).

$$X_i = \sum I_i \Big/ \left(\sum I_j + \sum I_k + \sum I_{l.....} \right), \quad \text{(Eq 1)}$$

where X_i = Fraction of i phase, $\sum I_i, \sum I_j, \sum I_k, \sum I_l$ = Cumulative intensities of i, j, k and l phase and Table 4 shows the individual phase fraction present in all three HEA cladding. As shown in Table 4, BCC phase is predominant compared to the FCC phase in all AlFeCuCrCoNi-WC_x HEA coating.

The outcomes revealed that additional phases in the cladding are restricted, and the laser-assisted rapid solidification process along with sluggish diffusion of HEA effectively avoids the precipitation of undesirable intermetallic compounds in the high-entropy alloy cladding. The Gibbs free energy of mixing was defined as follows:

$$\Delta G_{mix} = \Delta H_{mix} + T\Delta S_{mix} \quad \text{(Eq 2)}$$

This formula describes the relationship of Gibbs free energy (ΔG_{mix}), mixing enthalpy (ΔH_{mix}), mixing entropy (ΔS_{mix}) of the disordered solid solution. The mixing enthalpy of the system can be expressed by the Boltzmann approximation as follows (Ref 29):

$$\Delta S_{mix} = -R\left[C_1 \ln C_1 + C_1 \ln C_1 + C_1 \ln C_1 + \cdots + C_1 \ln C_1\right], \quad \text{(Eq 3)}$$

where R = Gas constant and C_n = Composition of the nth element. The equilibrium molar ratio of the constituents of the AlFeCuCrCoNi-WC_x causes a high enthalpy inside the alloy, which reduces the free energy of the alloy system and avoids the formation of intermetallic compound. Considering the

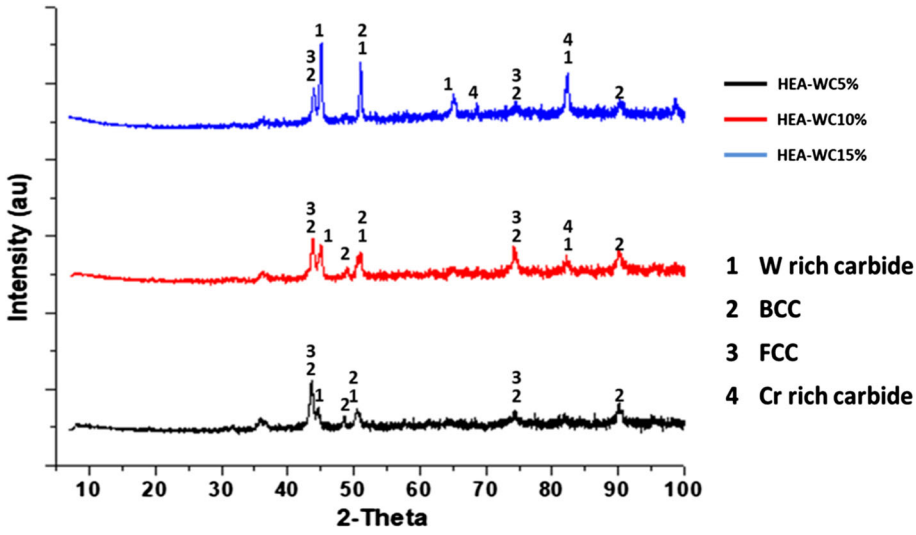

Fig. 2 XRD spectra of AlFeCuCrCoNi-WC_x high-entropy alloy cladding

Table 4 Phases and their fraction for AlFeCuCrCoNi-WC_x high-entropy alloy coating

Cladding	FCC fraction	BCC fraction	W-rich carbide	Cr-rich carbide
AlFeCuCrCoNi-WC_5	31.79	63.52	4.69	…
AlFeCuCrCoNi-WC_{10}	29.35	58.96	3.43	8.26
AlFeCuCrCoNi-WC_{15}	27.68	52.69	6.97	12.66

Table 5 Binary mixing enthalpies, $\Delta H^{mix}ij$ (kJ mol^{-1}) of principal elements with carbon

Elements	Al	Fe	Ni	Cu	Cr	Co	W
C	− 30	− 50	− 30	− 42	− 61	− 42	− 32

multiple overlap tracking (60% overlap) each layer in the present investigation is heated more than once and the carbide particles were completely dissolved. However, partial dissolution of the carbide particles can be helpful up to a certain point, as it provides a better bonding between the WC particles, HEA matrix, and precipitation of novel metal carbides. In contrast, if the reinforcing particles are completely dissolved, detrimental effects can take place, like porosity, due to the reaction of the released carbon atoms with the atmospheric oxygen-producing CO and CO_2 (Ref 8). As per Fig. 2 in addition to WC, other metal carbide was found in the cladding (AlFeCuCrCoNi-WC_{10} and AlFeCuCrCoNi-WC_{15}). It can be explained by the combined effect of both mixing enthalpy and entropy on the free energy of the multiple principle element alloy system. During partial deposition melting of WC takes place and WC is bifurcated as separate W and C. To determine their individual metal inclination to form carbides, the mixing enthalpies of Al, Fe, Cu, Cr, Co, Ni, and W with carbon are considered and shown in Table 5 (Ref 30).

The mixing enthalpy between metallic elements (Fe, Cu, Cr, and Co) and carbon is more negative than tungsten and carbon. In addition to that, the mixing enthalpy between carbon and chromium is the lowest among the possible carbide, so the additional metal carbide mostly consists of chromium-rich carbide. With increasing in the amount of WC, there is no change in phase composition of high-entropy alloy, but more content of chromium carbide is formed in high-entropy alloy coating. The peaks of Cr-rich carbide match with $Cr_{23}C_6$ (JCPDS: 35-0783) and not with Cr_2C_3 and Cr_7C_3 type carbides (Ref 31). However, the percentage contribution of carbon to form chromium-rich carbide was not sufficient in AlFeCuCrCoNi-WC_5 HEA cladding. As WC contribution in high-entropy alloy coating increased (10% and 15%), chromium-rich carbide form quite easily due to the availability of a high amount of carbon.

3.2 Microstructure

Figure 3 shows the microstructure of AlFeCuCrCoNi-WC_x (X = 5, 10, and 15%) HEA cladding developed with the aid of laser-assisted cladding process. The micrograph indicates that all three cladding is dense enough and free from pores, with a coating thickness of 0.9 mm. As shown in Fig. 3(a), (c), and (e), there are three typical regions in the cladding such as clad zone (CZ), bonding zone (BZ), and heat-affected zone (HAZ) depends on the variation in the microstructure. The clad layer microstructure is majorly composed of fine-grained nondirectional and equiaxed crystals away from the base material and columnar grains near to the base material. Furthermore, in-depth investigation for metallurgical characteristics of particular AlFeCuCrCoNi-WC_{10} high-entropy alloy coating is present in our previously published article (Ref 32). In accordance with the solidification theory, during the laser-cladding process, the liquid close to the base material has high-temperature gradient (ΔT), but the solidification rate (R) is less. Hence, the magnitude for the ratio of a temperature gradient to a solidification rate ($\Delta T/R$) is at the highest. So, the nucleation rate is much higher than the growth rate of the crystal (Ref 31). As solidification proceeds, the liquid–solid interface moves and tends to reduce temperature gradient (ΔT) and increase the solidification rate (R) (i.e., lower $\Delta T/R$ ratio). Then the grains grow rapidly in the cladding and producing columnar crystals. The columnar grains are transforming to equiaxed with a further reduction in a temperature gradient in the center of the cladding zone. The progression of the interface of the solid and liquid leads to an increase in the solidification rate. Contrary to which the temperature gradient decreases. This leads to the reduction in the value of $\Delta T/R$, which then transforms the cellular crystal to dendritic one. The cooling speed in the middle is generally slower; the grains have enough periods to grow in the direction of the flow of heat. As a result of this, the columnar crystals with a developed secondary dendrite arm are formed (Fig. 3a, c and e). Moving on with the solid and liquid interface, the melting layers is still far off from the substrate. Along with the continuous reducing value of $\Delta T/R$, further weakening can be indicated toward heat dissipation in perpendicular with the substance direction (Ref 33). As a result of this, the heat on either side of the pool is transferred, resulting in the lowering of the angle forming between the direction of the dendrites growth and the laser scanning resulting in the growth through all the directions (Fig. 3b, d, and f). Therefore, the laser cladding evolves the microstructure of HEA as cellular, cellular dendrite, columnar dendrite, and equiaxed dendrite. Under the criteria agreeing to the consultation undercooling during the laser-cladding process when the high-entropy alloy cools down, the difference in the temperature at the interface of solid–liquid along with the cooling rate is the major factors in the identification of the microstructure behavior of the high-entropy alloy. The curved line between the substrate and cladding indicates that there is an excellent metallurgical bond at the interface zone (Fig. 3a, c, and e). The growth direction of the columnar grain is perpendicular to the interface zone due to the rapid directional solidification of the laser-cladding process (Ref 30).

The composite coatings exhibited a continuous and smooth rippled appearance upon the addition of 5 wt.% WC particle, as shown in Fig. 3(b). The composite coating showed (Fig. 3d and c) a rough surface when the contribution of tungsten carbide reached 10wt.% and 15 wt.%, respectively. Furthermore, optical microscopy indicated fine cracks at the interface in the coatings having 10 wt.% and 15 wt.% tungsten carbide. The large variation in thermal expansion coefficient (μ) and density (ϱ) between HEA matrix (μ: 12.4 µm m^{-1} K^{-1}, ϱ: 7.1 g cm^{-3}), tungsten carbide (μ: 5.5 µm m^{-1} K^{-1}, ϱ: 15.6 g cm^{-3}) and substrate AISI 316 (μ: 16.0 µm m^{-1} K^{-1}, ϱ: 7.8 g cm^{-3}) could be the reason for formation of fine cracks at interface. It was revealed that the average grain size varies along with the variation in the contribution of tungsten carbide in the HEA matrix. The average grain size was nearly 20.6 µm when WC contribution was 5 wt.%, as shown in Fig. 3(b). The grains were refined and their average diameters could reach to 15 µm and 7.8 µm when WC contribution was 10 wt.% and 15 wt.%,

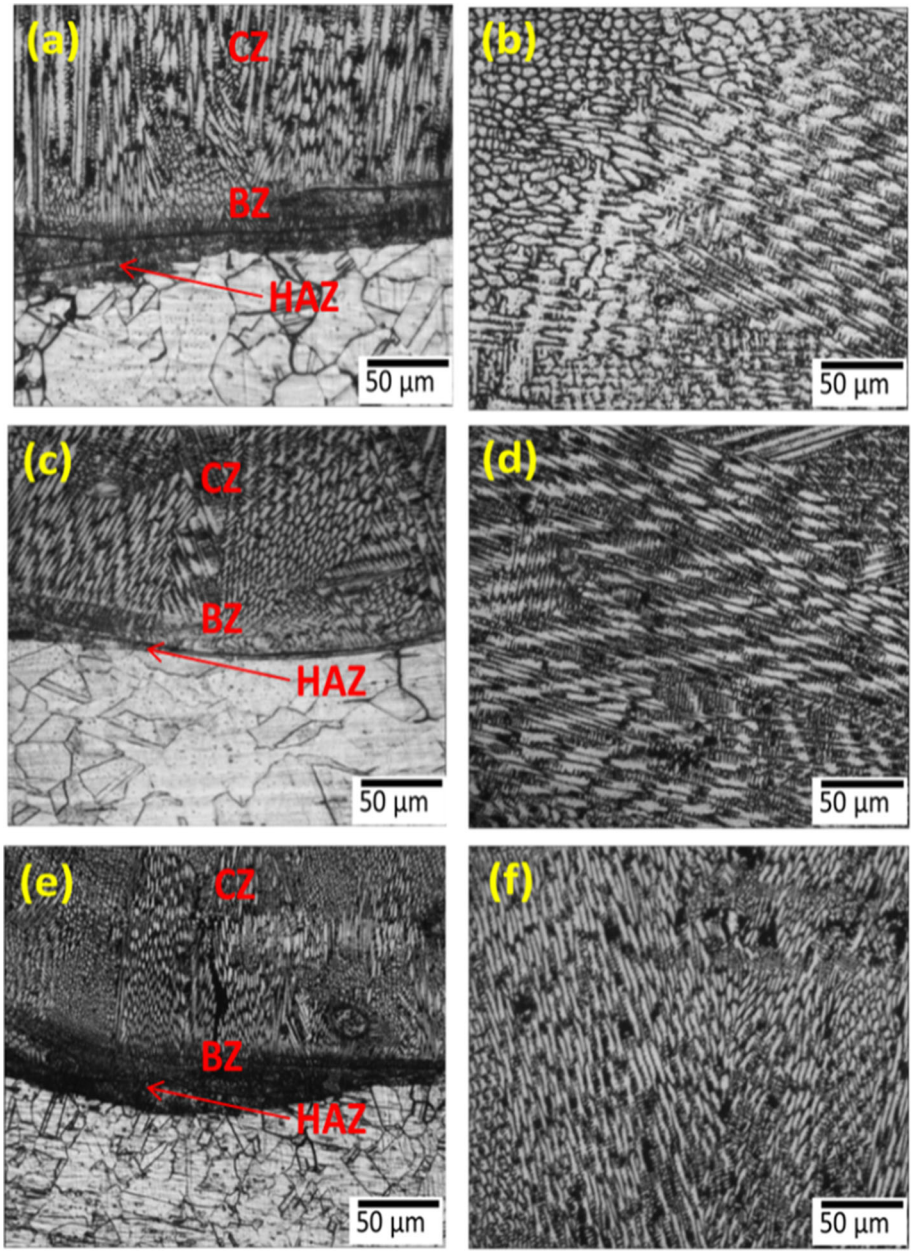

Fig. 3 Cross section optical microscopy images of the AlFeCuCrCoNi-WC_x high-entropy alloy coating. (a) Interface zone (x = 5%), (b) clad zone (x = 5%), (c) interface zone (x = 10%), (d) clad zone (x = 10%), (e) interface zone (x = 15%), (f) clad zone (x = 15%)

Table 6 EDS analysis results of various regions of AlFeCuCrCoNi-WC_x (X = 5, 10, and 15 wt.%) high-entropy alloy coating

Cladding	Region	Fe	Ni	Cr	Cu	Co	Al	W
AlFeCuCrCoNi-WC_5	Nominal composition	25.9	15.7	13.5	14.9	17.8	7.5	4.7
	Region A (ID)	27.7	14.9	12.2	9.9	12.5	6.9	15.9
	Region B (DR)	30.7	14.7	17.6	12.2	16.2	5.7	2.9
AlFeCuCrCoNi-WC_{10}	Nominal composition	23.7	14.8	13.8	16.7	15.9	6.2	8.9
	Region C (ID)	14.6	8.3	26.1	7.4	8.8	3.6	31.2
	Region D (DR)	29.1	16.1	13.2	15.2	15.3	5.2	5.9
AlFeCuCrCoNi-WC_{15}	Nominal composition	26.3	13.6	14.7	11.5	14.4	5.7	13.8
	Region E (ID)	11.3	9.5	29.2	5.6	5.1	2.5	36.8
	Region F (DR)	23.7	14.1	14.8	13.8	16.2	4.7	12.7

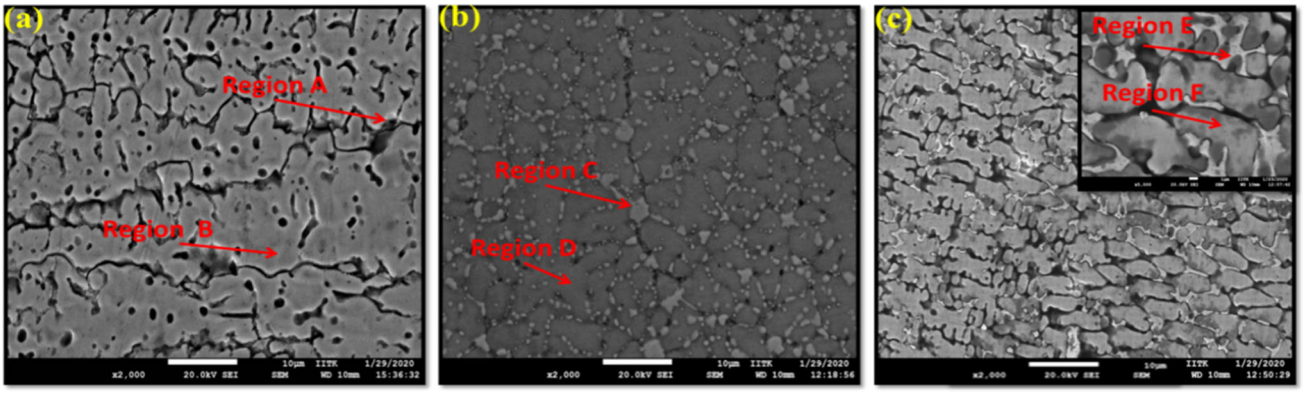

Fig. 4 High magnification FESEM images of the AlFeCuCrCoNi-WC_x high-entropy alloy coating, (a) AlFeCuCrCoNi-WC_5 (b) AlFeCuCrCoNi-WC_{10}, and (c) AlFeCuCrCoNi-WC_{15}

respectively. This was due to the addition of WC contributed to the heterogeneous nucleation during the process of setting by forming metal carbide (chromium carbide) (Ref 34, 35).

3.3 Compositional Analysis

Figure 4 indicates the high magnification FESEM images of AlFeCuCrCoNi-WC_x (X = 5, 10, and 15%) high-entropy alloy coatings. The energy dispersive spectroscopy quantitative results listed in Table 3 for all three coating along with various dendritic and inter-dendritic regions marked by arrow in Fig. 4. It was revealed that all the principal element was found to be uniformly distributed across the coating and individual contribution of primary elements was near to the designed weight percentage of the high-entropy alloy. Homogenous mixing of elemental powders, consistent and rapid deposition and solidification of laser-cladding and sluggish diffusion effect of high-entropy alloys might be the reason behind the uniform distribution of alloying elements. The dissolution of WC particles is majorly due to the capillary phenomena of melted material and concentrated laser energy, which may tend to the temperature of the cladding pool to go beyond the melting point of WC particles (Ref 34).The EDS analysis revealed that Fe content in the dendritic region is higher than that of the theoretical content. This is attributed to the rapid solidification and melting process of laser-cladding leads to melt and solidify small thin layer of AISI 316 (iron rich substrate) with the cladding layer. Figure 4 and Table 6 reveal that the weight fraction of chromium is increasing with an increase in WC percentage contribution in the inter-dendritic region due to the formation of chromium carbide. It can be seen that content of the element Cr and W in the inter-dendritic region (Region A, C, and E) is much more than that in the dendritic region (Region B, D, and F) in all three high-entropy alloy cladding. Furthermore, Fig. 5 shows the EDS elemental mapping for the individual elements in the cladding layer. As in area EDS analysis mapping also revealed the segregation of tungsten rich particles in the inter-dendritic region, while the other elements of the HEA are observed to be uniformly distributed throughout the cladding due to rapid melting solidification rate of laser-cladding process.

The W-rich carbide is directly from the reinforced WC particles. However, Cr-rich carbide is consequence of diffusion and reaction of tungsten and carbon with the high-entropy alloy matrix. The Cr-rich carbides are generally divided into three categories: $Cr_{23}C_6$, Cr_7C_3, and Cr_3C_2 in AlFeCuCrCoNi based high-entropy alloys in accordance with the following equations (Ref 31).

$$23Cr + 12WC \rightarrow Cr_{23}C_6 + 6W_2C \quad \text{(Eq 3)}$$

$$7Cr + 6WC \rightarrow Cr_7C_3 + 3W_2C \quad \text{(Eq 4)}$$

$$3Cr + 12WC \rightarrow Cr_3C_2 + 2W_2C \quad \text{(Eq 5)}$$

The Gibbs free energy was calculated for above equation. The formation of energies for $Cr_{23}C_6$, Cr_7C_3, and Cr_3C_2 are -368.59×10^3 J mol^{-1}, -169.54×10^3 J mol^{-1}, and -76.36×10^3 J mol^{-1}, respectively. Considering negative values of formation energies, it is likely to form all types of Cr-rich carbides under this condition. Furthermore, compared to the other types of Cr-rich carbides, the formation of $Cr_{23}C_6$ type carbide needs the lowest C content. Therefore, the Cr-rich carbides are mostly composed of $Cr_{23}C_6$ type carbide (Ref 31,32). On the other hand, the XRD spectra (Fig. 2) also confirm the presence of $Cr_{23}C_6$ along with WC phases. As mentioned earlier, the formation of chromium carbide is limited to the AlFeCuCrCoNi-WC_{10}, AlFeCuCrCoNi-WC_{15} high-entropy alloy coatings due to the insufficient presence of carbon content in AlFeCuCrCoNi-WC_5 high-entropy alloy coatings to form chromium carbide.

3.4 Microhardness

Figure 6 depicts the microhardness distribution for the synthesized AlFeCuCrCoNi-WC_x (x = 5, 10, and 15%) high-entropy alloy cladding along the cross section from the cladding zone to the AISI 316 substrate. The hardness of the cladding layer is much higher than that of the untreated substrate AISI 316. The variation in coating microstructure due to variation in composition is responsible for microhardness variation. The microhardness gradually increased with increasing percentage contribution of WC in high-entropy alloy coating. The peak hardness values for AlFeCuCrCoNi-WC_5, AlFeCuCrCoNi-WC_{10}, and AlFeCuCrCoNi-WC_{15} high-entropy alloy coating reaches to 326.8 $HV_{0.5}$, 622 $HV_{0.5}$, and 808.7 $HV_{0.5}$, respectively. Compared with that of the substrate AISI 316 (164.5 $HV_{0.5}$), the hardness of the claddings was enhanced by approximately 49.6%, 73.5%, and 79.7%, respectively. In the laser-assisted cladding process, quick melting, and solidification phenomena enhances the degree of solid solubil-

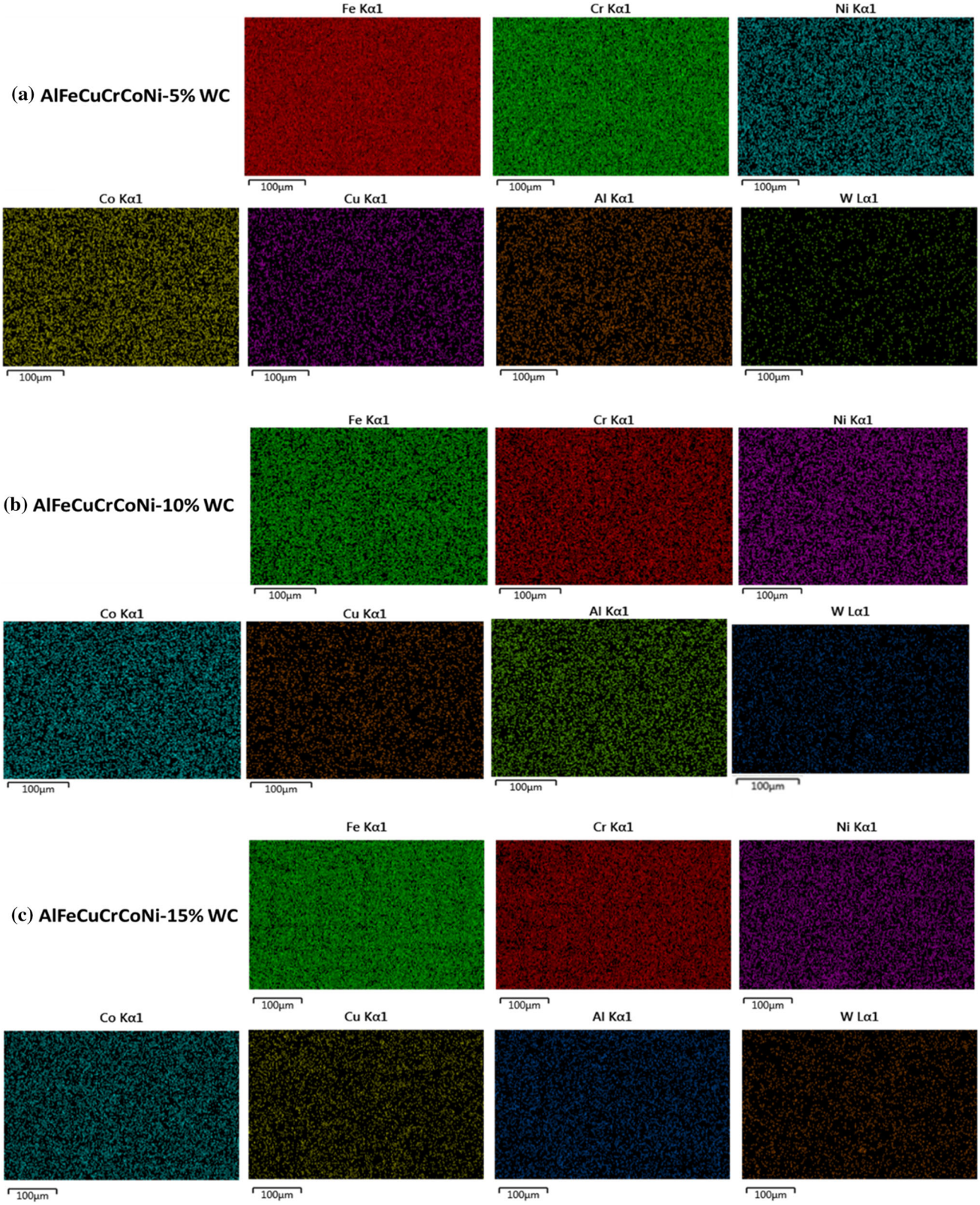

Fig. 5 EDS mapping of HEA cladding (a) AlFeCuCrCoNi-WC_5, (b) AlFeCuCrCoNi-WC_{10}, and (c) AlFeCuCrCoNi-WC_{15}

ity of the alloy, restricts grain growth, and initiates grain refinement results in solid solution strengthening and grain boundary strengthening, respectively. This increasing hardness is attributed to the combination of several reasons like substitutional solid solution strengthening, grain boundary strengthening, dispersion strengthening, interstitial solid solution strengthening, and precipitation hardening. The substitutional solid solution strengthening is important consideration

Table 7 Atomic radius of the individual element of the high-entropy alloy coating and variation in atomic radius between elemental pair

Elements	Al	Fe	Cu	Cr	Co	Ni	W	C
Atomic radius, nm	0.143	0.126	0.128	0.130	0.125	0.124	0.139	0.077
Al	…	0.017	0.015	0.013	0.018	0.019	0.004	0.066
Fe	0.017	…	0.002	0.004	0.001	0.002	0.013	0.049
Cu	0.015	0.002	…	0.002	0.003	0.004	0.011	0.051
Cr	0.013	0.004	0.002	…	0.005	0.006	0.009	0.053
Co	0.018	0.001	0.003	0.005	…	0.001	0.014	0.048
Ni	0.019	0.002	0.004	0.006	0.001	…	0.015	0.047
W	0.004	0.013	0.011	0.009	0.014	0.015	…	0.062
C	0.066	0.049	0.051	0.053	0.048	0.047	0.062	…

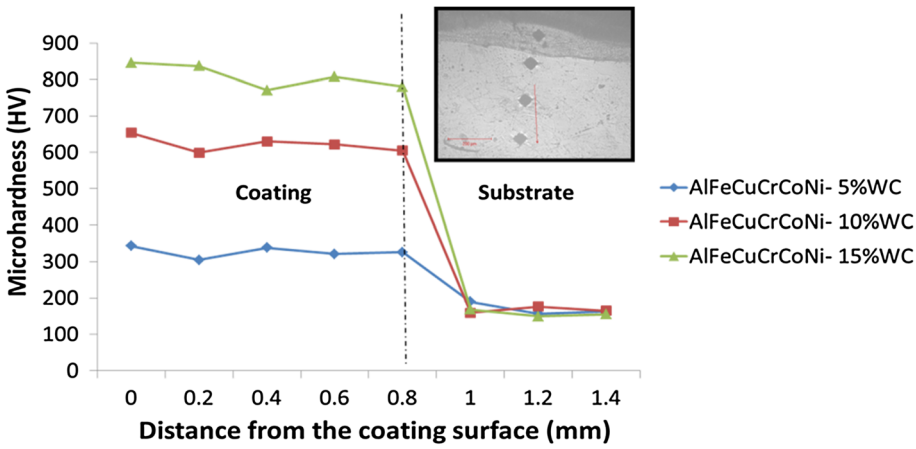

Fig. 6 Microhardness distribution of AlFeCuCrCoNi-WC_x high-entropy alloy coatings

Table 8 Electrochemical parameters of laser cladded and untreated AISI-316

Target material	$E_{corr.}$, mV	$I_{corr.}$, mA cm^{-2}	Corrosion rate, mil $year^{-1}$	Corrosion rate, g h^{-1}
AISI 316	− 119	2.20×10^{-3}	9.91×10^{2}	2.32×10^{-3}
AlFeCuCrCoNi-WC_5	− 110	1.04×10^{-3}	5.23×10^{2}	1.03×10^{-3}
AlFeCuCrCoNi-WC_{10}	− 108	1.14×10^{-3}	5.82×10^{2}	1.13×10^{-3}
AlFeCuCrCoNi-WC_{15}	− 135	1.58×10^{-3}	8.05×10^{2}	1.57×10^{-3}

since all the elemental atoms forming high-entropy alloy coating in the solid solution could be regarded as the solute or solvent atoms the larger atomic size difference between metallic elements lead to more sever lattice distortion and solution strengthening. The larger atomic size difference of W and Al will lead to more severe lattice distortion and hence more powerful solution strengthening as indicated in Table 7 (Ref 35,36). The rapid cooling rate as in laser-cladding results in grain refinement and contributes to Grain boundary strengthening (In accordance to Hall Petch Equation: $\sigma_y = \sigma_o + (k_y/d^{1/2})$, where k_y = strengthening coefficient, σ_y = yield stress, σ_o = materials constant and d = grain diameter).

The presence of WC in HEA has manifolds effects. Firstly, the partial dissolution of WC ensures good adhesion to the substrate. Additionally, free carbon of WC tends to combine with elements having a negative enthalpy of mixing and formation of in situ coherent carbides leads to precipitation hardening. This in situ coherent metal carbides and undissolved WC (dispersion strengthening) act as a nucleating site for grain resulting in grain refinement. Microstructure results revealed that increasing in WC contribution leads refinement in the grain size. Subsequently, the average microhardness magnitudes of the AlFeCuCrCoNi-WC_x high-entropy alloy cladding layers are much higher than that of the substrate AISI 316 (Ref 37,38).

3.5 Electrochemical Behavior

The microstructure and composition are the key factors to determine the corrosion behavior of multi-principle elements alloy coatings. However, these alloys also rely on the interactions between compositional elements and reinforcements, which can play an important role in the overall properties (Ref 38,39). In the Cl^- containing corrosive solution pitting susceptibility, a property of the passive film and pitting resistance is significantly affected by the surface roughness of the target material (Ref 40). Therefore, prior to electrochemical testing, the surface of the coating was made smooth and the average surface roughness was kept approximately 3 µm. The potentiodynamic polarization curves (Tafel plot) of untreated substrate AISI 316, AlFeCuCrCoNi-WC_5, AlFeCuCrCoNi-WC_{10}, and AlFeCuCrCoNi-WC_{15} high-entropy alloy cladded substrate in 3.5 wt.% NaCl solution at room temperature are

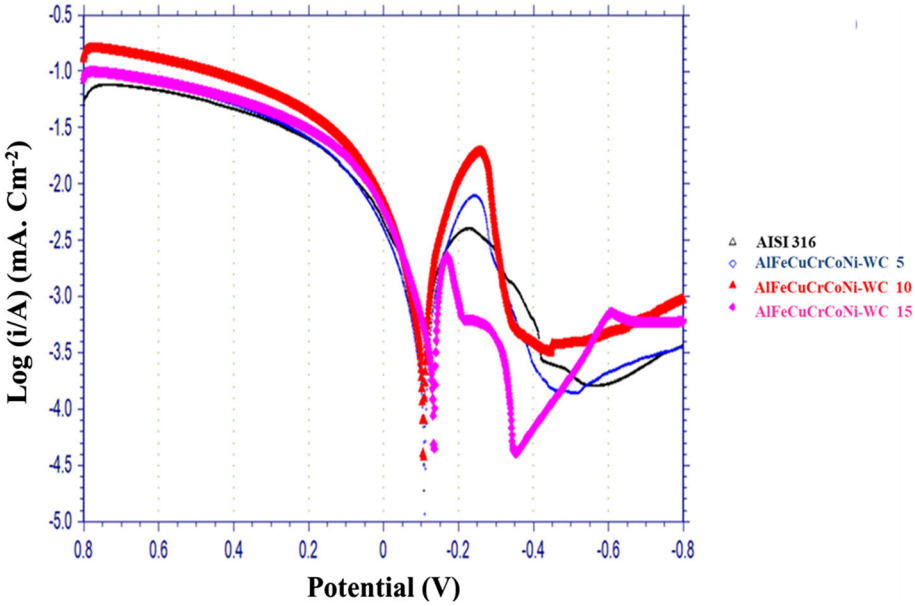

Fig. 7 Potentiodynamic polarization curves (Tafel plot) of untreated AISI 316 substrate and AlFeCuCrCoNi-WC_x high-entropy alloy coatings

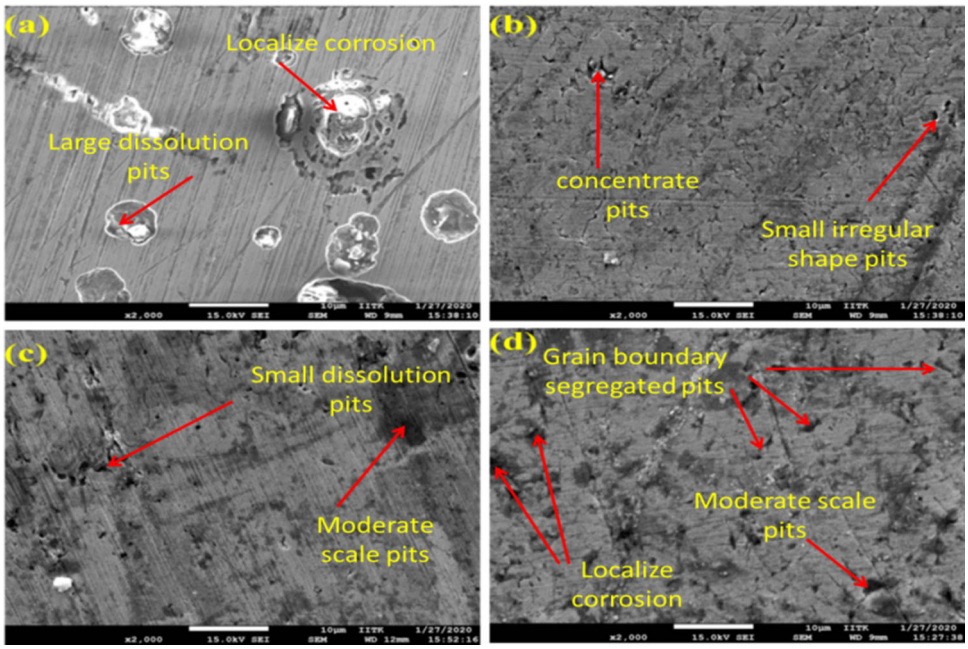

Fig. 8 Corroded surface morphology of (a) Substrate AISI 316, (b) AlFeCuCrCoNi-WC_5, (c) AlFeCuCrCoNi-WC_{10}, and (d) AlFeCuCrCoNi-WC_{10}

indicated in Fig. 7. Table 8 shows the values of electrochemical parameters, such as corrosion potential (Ecorr.), corrosion current density ($I_{corr.}$), and corrosion rate for AlFeCuCrCoNi-WC_x HEA coating and untreated base material AISI 316 extracted from potentiodynamic polarization curve.

As shown in Table 8, the values of corrosion potential (Ecorr) achieved in close range. At the same time, there were a marginal difference observed in corrosion current (Icorr) values of high-entropy alloy coatings (AlFeCuCrCoNi-WC_x) and substrate AISI 316. The magnitude of corrosion potential for the AISI 316 substrate, AlFeCuCrCoNi-WC_5, AlFeCuCrCoNi-WC_{10}, and AlFeCuCrCoNi-WC_{15} high-entropy alloy cladding are -111 mV, -110mV, -108mV, and -135mV, respectively. While, the corrosion current density of untreated steel substrate, AlFeCuCrCoNi-WC_5, AlFeCuCrCoNi-WC_{10}, and AlFeCuCrCoNi-WC_{15} high-entropy alloy cladding are 2.20×10^{-3} mA cm^{-2}, 1.04×10^{-3} mA cm^{-2}, 1.14×10^{-3} mA cm^{-2}, and 1.58×10^{-3} mA cm^{-2}, respectively. Compared to the substrate (AISI-316), the AlFeCuCrCoNi-WC_x high-entropy alloy coatings free corrosion current density is reduced, and free corrosion potential is more "positive." This relationship between electrochemical parameters reveals that all three

high-entropy alloy cladding on AISI 316 substrate can protect it in 3.5 wt.% NaCl corrosive environment. Considering the present corrosion behavior of high-entropy alloy coating in 3.5 wt.% NaCl, the passivation process of alloy in the anodic region by assimilation of water molecules on the surface of a metal is hindered due to the presence of Cl^- ions. When a protective film is formed on the surface of the alloy, Cl^- will aggregate on the protective membrane interface and enter the membrane to contact with the alloy surface fully, so as to accelerate the corrosion of the alloy (Ref 41–44). The existence of corrosion-resistant specific elements like nickel, chromium, and cobalt and lower aluminum content plays crucial role in the good corrosion performance of the AlFeCuCrCoNi-WC_x ($x = 5$, 10, and 15%) high-entropy alloy coatings.

The reduction in corrosion resistivity of high-entropy alloy cladding with an increase in the contribution of WC is attributed to one or a combination of the following reasons. As the microstructural studies reveal that increment in WC contribution in high-entropy alloy coating tends to reduce grain size from 20.6 to 7.8 µm. The effect is related to the fact that finer grains increase the surface area of the interfaces and could enhance the formation of micro-galvanic couples in the cladding material. The formation of a galvanic couple between grain interface leads to degrading the corrosion performance of the coating. This phenomenon is also observed by Ziejewska et al. (Ref 45).

On the other hand, increasing the weight fraction of WC in the high-entropy alloy cladding tends to form chromium carbide ($Cr_{23}C_6$) in the inter-dendritic zone. The formation of metal carbide leads to reduce chromium weight fraction in the dendritic zone (HEA phase). Therefore, less amount of Cr_2O_3 corrosion resistance passive films form due to insufficient presence of chromium contains in the HEA phase of AlFeCuCrCoNi-WC_{10} and AlFeCuCrCoNi-WC_{10} high-entropy alloy coatings.

Furthermore, FESEM observations (Fig. 8) for the corroded morphology of the sample clearly elucidate the results extracted from Tafel plot. According to the corroded surface morphology, the primary corrosion mechanism was mainly localized corrosion and pitting, not uniform corrosion. As shown in Fig. 8(b), (c), and (d) corroded surface of AlFeCuCrCoNi-WC_x HEA cladding showed various small irregular shapes of dissolution pits. In contrast, the corroded surface of substrate AISI 316 (Fig. 8a) showed larger dissolution pits as compared to laser cladded specimens. But the corroded surface of AlFeCuCrCoNi-WC_x high-entropy alloy coatings indicates that an increase in the contribution of WC tend to increase dissolution pits and progressively deteriorate the corrosion performance of the coating.

4. Conclusion

The attempt was made to synthesize AlFeCuCrCoNi-WC_x high-entropy alloy coating on AISI 316 substrate. The influence of WC elements on their phase constituent, microstructure, microhardness and corrosion performance has been briefly investigated, and the major conclusions can be drawn as follows:

a. The crystal structures of AlFeCuCrCoNi-WC_x high-entropy alloy coatings evolved from FCC + BCC + WC phases for $X = 5\%$ and FCC + BCC + WC + $Cr_{23}C_6$ phases for $X = 10$ and 15%, respectively. On the other hand, intensities of diffraction peaks WC and $Cr_{23}C_6$ increase with increasing in WC contribution to HEA matrix.
b. The microstructure results revealed that AlFeCuCrCoNi-WC_x HEA coating is mainly composed of fine-grained nondirectional and equiaxed crystals away from the base material and columnar grains near to the base material. It is also concluded that increasing in WC element contribution leads to reduce grain size. The formation of chromium carbide is limited to the AlFeCuCrCoNi-WC_{10} AlFeCuCrCoNi-WC_{15} high-entropy alloy coatings due to the insufficient presence of carbon content in AlFeCuCrCoNi-WC_5 high-entropy alloy coatings to form chromium carbide.
c. As compared to the substrate AISI 316 (164.5 $HV_{0.5}$), the hardness of the AlFeCuCrCoNi-WC_5, AlFeCuCrCoNi-WC_{10}, and AlFeCuCrCoNi-WC_{15} claddings was enhanced by approximately 49.6, 73.5, and 79.7%, respectively.
d. The corrosion resistance performance of the AlFeCuCrCoNi-WC_x HEA coating in 3.5 wt.% NaCl corrosive environment is better than that of the substrate AISI 316. Consequently, the corrosion rate of the high-entropy alloy coating increases and corrosion resistance is degraded with the rise in WC contribution in HEA matrix. The corroded surface of AlFeCuCrCoNi-WC_x HEA cladding showed various small irregular shapes of dissolution pits. In contrast, the corroded surface of substrate AISI 316 showed larger dissolution pits as compared to laser cladded specimens.

Acknowledgments

The author appreciates the funding provided by the Department of Science and Technology, India (DST-EMR/2016/000451) and ACMS Department of IIT-Kanpur for metallurgical characterization.

References

1. H. Dong, Y. Sun, and T. Bell, Enhanced Corrosion Resistance of Duplex Coatings, *Surf. Coat. Technol.*, 1997, **90**(1–2), p 91–101. https://doi.org/10.1016/S0257-8972(96)03099-X
2. J.H. Zhao, X.L. Ji, Y.P. Shan, Y. Fu, and Z. Yao, On the Microstructure and Erosion-Corrosion Resistance of AlCrFeCoNiCu High-Entropy Alloy via Annealing Treatment, *Mater. Sci. Technol. (U. K.)*, 2016, **32** (12), p 1271–1275. https://doi.org/10.1080/02670836.2015.1116494
3. J. Mehta, V.K. Mittal, and P. Gupta, Role of Thermal Spray Coatings on Wear, Erosion and Corrosion Behavior: A Review, *J. Appl. Sci. Eng.*, 2017, **20**(4), p 445–452. https://doi.org/10.6180/jase.2017.20.4.05
4. O.S. Fatoba, P.A.I. Popoola, S.L. Pityana, and O.S. Adesina, Computational Dynamics of Anti-corrosion Performance of Laser Alloyed Metallic Materials, *Fiber Laser*, 2016 https://doi.org/10.5772/62334
5. H. Zhang, Y. Pan, Y. He, and H. Jiao, Microstructure and Properties of 6FeNiCoSiCrAlTi High-Entropy Alloy Coating Prepared by Laser Cladding, *Appl. Surf. Sci.*, 2011, **257**(6), p 2259–2263. https://doi.org/10.1016/j.apsusc.2010.09.084
6. S. Sun, Y. Durandet,and M. Brandt, Parametric Investigation of Pulsed Nd: YAG Laser Cladding of Stellite 6 on Stainless Steel, *Surf. Coat. Technol.*, 2005, **194**(2–3), p 225–231. https://doi.org/10.1016/j.surfcoat.2004.03.058

7. J.B. Cheng, X.B. Liang, Z.H. Wang, and B.S. Xu, Formation and Mechanical Properties of Conicufecr High-Entropy Alloys Coatings Prepared by Plasma Transferred Arc Cladding Process, *Plasma Chem. Plasma Process.*, 2013, **33**(5), p 979–992. https://doi.org/10.1007/s11090-013-9469-1
8. T.K. Chen, T.T. Shun, J.W. Yeh, and M.S. Wong, Nanostructured Nitride Films of Multi-Element High-Entropy Alloys by Reactive DC Sputtering, *Surf. Coat. Technol.*, 2004, **188–189**, p 193–200. https://doi.org/10.1016/j.surfcoat.2004.08.023
9. Y. Guo, X. Shang, and Q. Liu, Microstructure and Properties of In-Situ TiN Reinforced Laser Cladding CoCr2FeNiTix High-Entropy Alloy Composite Coatings, *Surf. Coat. Technol.*, 2018, **344**, p 353–358. https://doi.org/10.1016/j.surfcoat.2018.03.035
10. C. Ni, Y. Shi, J. Liu, and G. Huang, Characterization of Al0.5Fe-Cu0.7NiCoCr High-Entropy Alloy Coating on Aluminum Alloy by Laser Cladding, *Opt. Laser Technol.*, 2018, **105**, p 257–263. https://doi.org/10.1016/j.optlastec.2018.01.058
11. X. Wu Qiu, M. Jun Wu, C. Ge Liu, Y. Peng Zhang, and C. Xiang Huang, Corrosion Performance of Al2CrFeCoxCuNiTi High-Entropy Alloy Coatings in Acid Liquids, *J. Alloys Compd.*, 2017, **708**, p 353–357. https://doi.org/10.1016/j.jallcom.2017.03.054
12. F. Shu, B. Yang, S. Dong, H. Zhao, B. Xu, F. Xu, B. Liu, P. He, and J. Feng, Effects of Fe-to-Co Ratio on Microstructure and Mechanical Properties of Laser Cladded FeCoCrBNiSi High-Entropy Alloy Coatings, *Appl. Surf. Sci.*, 2018, **450**, p 538–544. https://doi.org/10.1016/j.apsusc.2018.03.128
13. C.L. Wu, S. Zhang, C.H. Zhang, H. Zhang, and S.Y. Dong, Phase Evolution and Cavitation Erosion-Corrosion Behavior of FeCoCrAlNiTixhigh Entropy Alloy Coatings on 304 Stainless Steel by Laser Surface Alloying, *J. Alloys Compd.*, 2017, **698**, p 761–770. https://doi.org/10.1016/j.jallcom.2016.12.196
14. W.L. Hsu, Y.C. Yang, C.Y. Chen, and J.W. Yeh, Thermal Sprayed High-Entropy NiCo0.6Fe0.2Cr1.5SiAlTi0.2 Coating with Improved Mechanical Properties and Oxidation Resistance, *Intermetallics*, 2017, **89**(May), p 105–110. https://doi.org/10.1016/j.intermet.2017.05.015
15. C.J. Tong, M.R. Chen, S.K. Chen, J.W. Yeh, T.T. Shun, S.J. Lin, and S. Y. Chang, Mechanical Performance of the AlxCoCrCuFeNi High-Entropy Alloy System with Multiprincipal Elements, *Metall. Mater. Trans. A Phys. Metall. Mater. Sci.*, 2005, **36**(5), p 1263–1271. https://doi.org/10.1007/s11661-005-0218-9
16. Y. Zhang, T. Zuo, Y. Cheng, and P.K. Liaw, High-Entropy Alloys with High Saturation Magnetization, Electrical Resistivity, and Malleability, *Sci. Rep.*, 2013, **3**, p 1–7
17. S. Varalakshmi, G. Appa Rao, M. Kamaraj, and B.S. Murty, Hot Consolidation and Mechanical Properties of Nanocrystalline Equiatomic AlFeTiCrZnCu High Entropy Alloy after Mechanical Alloying, *J. Mater. Sci.*, 2010, **45**(19), p 5158–5163. https://doi.org/10.1007/s10853-010-4246-5
18. K.B. Zhang, Z.Y. Fu, J.Y. Zhang, J. Shi, W.M. Wang, H. Wang, Y.C. Wang, and Q.J. Zhang, Annealing on the Structure and Properties Evolution of the CoCrFeNiCuAl High-Entropy Alloy, *J. Alloys Compd.*, 2010, **502**(2), p 295–299. https://doi.org/10.1016/j.jallcom.2009.11.104
19. Y.P. Wang, B.S. Li, M.X. Ren, C. Yang, and H.Z. Fu, Microstructure and Compressive Properties of AlCrFeCoNi High Entropy Alloy, *Mater. Sci. Eng. A*, 2008, **491**(1–2), p 154–158. https://doi.org/10.1016/j.msea.2008.01.064
20. Q. Chao, T. Guo, T. Jarvis, X. Wu, P. Hodgson, and D. Fabijanic, Direct Laser Deposition Cladding of AlxCoCrFeNi High Entropy Alloys on a High-Temperature Stainless Steel, *Surf. Coat. Technol.*, 2017, **332**(May), p 440–451. https://doi.org/10.1016/j.surfcoat.2017.09.072
21. Y. Peng, W. Zhang, T. Li, M. Zhang, B. Liu, Y. Liu, L. Wang, and S. Hu, Effect of WC Content on Microstructures and Mechanical Properties of FeCoCrNi High-Entropy Alloy/WC Composite Coatings by Plasma Cladding, *Surf. Coat. Technol.*, 2020, **385**, p 125326. https://doi.org/10.1016/j.surfcoat.2019.125326
22. S. Zhu, Y. Yu, B. Zhang, Z. Zhang, X. Yan, and Z. Wang, Microstructure and Wear Behaviour of In-Situ TiN-Al_2O_3 Reinforced CoCrFeNiMn High-Entropy Alloys Composite Coatings Fabricated by Plasma Cladding, *Mater. Lett.*, 2020, **272**, p 127870. https://doi.org/10.1016/j.matlet.2020.127870
23. I.L. Velo, F.J. Gotor, M.D. Alcalá, C. Real, and J.M. Córdoba, Fabrication and Characterization of WC-HEA Cemented Carbide Based on the CoCrFeNiMn High Entropy Alloy, *J. Alloys Compd.*, 2018, **746**, p 1–8. https://doi.org/10.1016/j.jallcom.2018.02.292
24. X.W. Qui, Microstructure and Properties of AlCrFeNiCoCu High Entropy Alloy Prepared by Powder Metallurgy, *J. Alloys Compd.*, 2013, **555**, p 246–249. https://doi.org/10.1016/j.jallcom.2012.12.071
25. P.K. Rai, S. Shekhar, K. Yagi, K. Ameyama, and K. Mondal, Corrosion Behavior of Harmonic Structured 316L Stainless Steel in 3.5% NaCl and Simulated Body Fluid Solution, *J. Mater. Eng. Perform.*, 2019, **28**(12), p 7554–7564. https://doi.org/10.1007/s11665-019-04428-x
26. Y.B. Peng, W. Zhang, X.L. Mei, H.J. Wang, M.Y. Zhang, L. Wang, X. F. Li, and Y. Hu, Microstructures and Mechanical Properties of FeCoCrNi-Mo High Entropy Alloys Prepared by Spark Plasma Sintering and Vacuum Hot-Pressed Sintering, *Mater. Today Commun.*, 2020, **24**, p 101009. https://doi.org/10.1016/j.mtcomm.2020.101009
27. D. Tanigawa, N. Abe, M. Tsukamoto, Y. Hayashi, H. Yamazaki, Y. Tatsumi, and M. Yoneyama, Effect of Laser Path Overlap on Surface Roughness and Hardness of Layer in Laser Cladding, *Sci. Technol. Weld. Join.*, 2015, **20**(7), p 601–606. https://doi.org/10.1179/1362171815Y.0000000044
28. C.J. Tong, Y.L. Chen, S.K. Chen, J.W. Yeh, T.T. Shun, C.H. Tsau, S.J. Lin, and S.Y. Chang, Microstructure Characterization of AlxCoCrCu-FeNi High-Entropy Alloy System with Multiprincipal Elements, *Metall. Mater. Trans. A Phys. Metall. Mater. Sci.*, 2005, **36**(4), p 881–893. https://doi.org/10.1007/252Fs11661-005-0283-0
29. R. Sriharitha, B.S. Murty, and R.S. Kottada, Phase Formation in Mechanically Alloyed Al XCoCrCuFeNi (x = 0.45, 1, 2.5, 5 Mol) High Entropy Alloys, *Intermetallics*, 2013, **32**, p 119–126. https://doi.org/10.1016/j.intermet.2012.08.015
30. Y.B. Peng, W. Zhang, T.C. Li, M.Y. Zhang, L. Wang, Y. Song, S.H. Hu, and Y. Hu, Microstructures and Mechanical Properties of FeCoCrNi High Entropy Alloy/WC Reinforcing Particles Composite Coatings Prepared by Laser Cladding and Plasma Cladding, *Int. J. Refract. Met. Hard Mater.*, 2019, **84**, p 1–9. https://doi.org/10.1016/j.ijrmhm.2019.105044
31. R. Zhou, G. Chen, B. Liu, J. Wang, L. Han, and Y. Liu, Microstructures and Wear Behaviour of (FeCoCrNi)1–x(WC)x High Entropy Alloy Composites, *Int. J. Refract. Met. Hard Mater.*, 2018, **75**(April), p 56–62. https://doi.org/10.1016/j.ijrmhm.2018.03.019
32. A. Vyas, J. Menghani, and H. Natu, Metallurgical and Mechanical Properties of Laser Cladded AlFeCuCrCoNi-WC10 High Entropy Alloy Coating, *Int. J. Eng.*, 2020, **33**(7), p 1397–1402
33. S. Gorsse, M.H. Nguyen, O.N. Senkov, and D.B. Miracle, Database on the Mechanical Properties of High Entropy Alloys and Complex Concentrated Alloys, *Data Br.*, 2018, **21**, p 2664–2678. https://doi.org/10.1016/j.dib.2018.11.111
34. C. Shang, E. Axinte, W. Ge, Z. Zhang, and Y. Wang, High-Entropy Alloy Coatings with Excellent Mechanical, Corrosion Resistance and Magnetic Properties Prepared by Mechanical Alloying and Hot Pressing Sintering, *Surf. Interfaces*, 2016, **2017**(9), p 36–43. https://doi.org/10.1016/j.surfin.2017.06.012
35. S. Zhang, C.L. Wu, J.Z. Yi, and C.H. Zhang, Synthesis and Characterization of FeCoCrAlCu High-Entropy Alloy Coating by Laser Surface Alloying, *Surf. Coat. Technol.*, 2015, **262**, p 64–69. https://doi.org/10.1016/j.surfcoat.2014.12.013
36. W. Luo, Y. Liu, Y. Luo, and M. Wu, Fabrication and Characterization of WC-AlCoCrCuFeNi High-Entropy Alloy Composites by Spark Plasma Sintering, *J. Alloys Compd.*, 2018, **754**, p 163–170. https://doi.org/10.1016/j.jallcom.2018.04.270
37. W. Luo, Y. Liu, and J. Shen, Effects of Binders on the Microstructures and Mechanical Properties of Ultrafine WC-10%AlxCoCrCuFeNi Composites by Spark Plasma Sintering, *J. Alloys Compd.*, 2019, **791**, p 540–549. https://doi.org/10.1016/j.jallcom.2019.03.328
38. H. Luo, S. Zou, Y.H. Chen, Z. Li, C. Du, and X. Li, Influence of Carbon on the Corrosion Behaviour of Interstitial Equiatomic CoCrFeMnNi High-Entropy Alloys in a Chlorinated Concrete Solution, *Corros. Sci.*, 2020, **163**, p 108287. https://doi.org/10.1016/j.corsci.2019.108287
39. X. Yang, X. Li, Q. Yang, H. Wei, X. Fu, and W. Li, Effects of WC on Microstructure and Corrosion Resistance of Directional Structure Ni60 Coatings, *Surf. Coat. Technol.*, 2020, **385**, p 125359. https://doi.org/10.1016/j.surfcoat.2020.125359
40. L. Wei, Y. Liu, Q. Li, and Y.F. Cheng, Effect of Roughness on General Corrosion and Pitting of (FeCoCrNi)0.89(WC)0.11 High-Entropy Alloy Composite in 3.5 Wt% NaCl Solution, *Corros. Sci.*, 2019, **146**, p 44–57. https://doi.org/10.1016/j.corsci.2018.10.025

41. Y. Kuan Zhou, X. Bin Liu, J. Jie Kang, W. Yue, W. Bo Qin, G. Zheng Ma, Z. Qiang Fu, L. Na Zhu, D. Shun She, H. Dou Wang, J. Liang, W. Weng, and C. Biao Wang, Corrosion Behavior of HVOF Sprayed WC-10Co4Cr Coatings in the Simulated Seawater Drilling Fluid Under the High Pressure, *Eng. Fail. Anal.*, 2020, **109**, p 104338. https://doi.org/10.1016/j.engfailanal.2019.104338
42. W. Qiu, Y. Liu, J. Ye, H. Fan, and Y. Qiu, Effects of (Ti, Ta, Nb, W)(C, N) on the Microstructure, Mechanical Properties and Corrosion Behaviors of WC-Co Cemented Carbides, *Ceram. Int.*, 2017, **43**(3), p 2918–2926. https://doi.org/10.1016/j.ceramint.2016.09.124
43. C. Yi, H. Fan, J. Xiong, Z. Guo, G. Dong, W. Wan, and H. Chen, Effect of WC Content on the Microstructures and Corrosion Behavior of Ti(C, N)-Based Cermets, *Ceram. Int.*, 2013, **39**(1), p 503–509. https://doi.org/10.1016/j.ceramint.2012.06.055
44. F.J.J. Kellner, H. Hildebrand, and S. Virtanen, Effect of WC Grain Size on the Corrosion Behavior of WC-Co Based Hardmetals in Alkaline Solutions, *Int. J. Refract. Met. Hard Mater.*, 2009, **27**(4), p 806–812. https://doi.org/10.1016/j.ijrmhm.2009.02.004
45. C. Ziejewska, J. Marczyk, A. Szewczyk-Nykiel, M. Nykiel, and M. Hebda, Influence of Size and Volume Share of WC Particles on the Properties of Sintered Metal Matrix Composites, *Adv. Powder Technol. Soc. Powder Technol. Jpn.*, 2019, **30**(4), p 835–842. https://doi.org/10.1016/j.apt.2019.01.013